


ORIGINAL RESEARCH

Open Access



# Impact of segmentation and discretization on radiomic features in $^{68}\text{Ga}$ -DOTA-TOC PET/CT images of neuroendocrine tumor

Virginia Liberini<sup>1\*</sup> , Bruno De Santi<sup>2</sup>, Osvaldo Rampado<sup>3</sup>, Elena Gallio<sup>3</sup>, Beatrice Dionisi<sup>1</sup>, Francesco Ceci<sup>1</sup>, Giulia Polverari<sup>1</sup>, Philippe Thuillier<sup>1,4</sup>, Filippo Molinari<sup>2</sup> and Désirée Deandreis<sup>1</sup>

\* Correspondence: [virginia.liberini@unito.it](mailto:virginia.liberini@unito.it)

<sup>1</sup>Nuclear Medicine Unit, Department of Medical Sciences, University of Turin, Corso Dogliotti 14, 10126 Turin, Italy

Full list of author information is available at the end of the article

## Abstract

**Objective:** To identify the impact of segmentation methods and intensity discretization on radiomic features (RFs) extraction from  $^{68}\text{Ga}$ -DOTA-TOC PET images in patients with neuroendocrine tumors.

**Methods:** Forty-nine patients were retrospectively analyzed. Tumor contouring was performed manually by four different operators and with a semi-automatic edge-based segmentation (SAEB) algorithm. Three  $\text{SUV}_{\text{max}}$  fixed thresholds (20, 30, 40%) were applied. Fifty-one RFs were extracted applying two different intensity rescale factors for gray-level discretization: one absolute ( $\text{AR60} = \text{SUV}$  from 0 to 60) and one relative ( $\text{RR} = \text{min-max}$  of the VOI  $\text{SUV}$ ). Dice similarity coefficient (DSC) was calculated to quantify segmentation agreement between different segmentation methods. The impact of segmentation and discretization on RFs was assessed by intra-class correlation coefficients (ICC) and the coefficient of variance ( $\text{COV}^2$ ). The RFs' correlation with volume and  $\text{SUV}_{\text{max}}$  was analyzed by calculating Pearson's correlation coefficients.

**Results:** DSC mean value was  $0.75 \pm 0.11$  (0.45–0.92) between SAEB and operators and  $0.78 \pm 0.09$  (0.36–0.97), among the four manual segmentations. The study showed high robustness ( $\text{ICC} > 0.9$ ): (a) in 64.7% of RFs for segmentation methods using AR60, improved by applying  $\text{SUV}_{\text{max}}$  threshold of 40% (86.5%); (b) in 50.9% of RFs for different  $\text{SUV}_{\text{max}}$  thresholds using AR60; and (c) in 37% of RFs for discretization settings using different segmentation methods. Several RFs were not correlated with volume and  $\text{SUV}_{\text{max}}$ .

**Conclusions:** RFs robustness to manual segmentation resulted higher in NET  $^{68}\text{Ga}$ -DOTA-TOC images compared to  $^{18}\text{F}$ -FDG PET/CT images. Forty percent  $\text{SUV}_{\text{max}}$  thresholds yield superior RFs stability among operators, however leading to a possible loss of biological information. SAEB segmentation appears to be an optimal alternative to manual segmentation, but further validations are needed. Finally, discretization settings highly impacted on RFs robustness and should always be stated.

**Keywords:** Texture analysis, Radiomics, Neuroendocrine tumor, Robustness,  $^{68}\text{Ga}$ -DOTATOC PET/CT, Semi-automatic segmentation

## Introduction

Neuroendocrine tumors (NET) are a heterogeneous group of malignancies represented by different histological subtypes and different primary locations [1]. Histopathology is crucial in tumor classification and Ki-67 is currently used to define tumor grading in GEP NET [2]. However, the assessment of tumor aggressiveness is generally assessed by lesion biopsy, leading to a potential grading underestimation [3], since tumor heterogeneity is both spatial (inter- and intra-tumoral heterogeneity) and time-related (more aggressive cell clones developing over time) [4, 5]. Thus, although multiple-lesion biopsy sampling is not feasible, grading heterogeneity among primary and secondary lesions is not negligible [6]. New generation imaging technologies, including positron emission tomography (PET), might offer its contribution in the evaluation of tumor heterogeneity [7–9]. At present, PET imaging with  $^{68}\text{Ga}$ -DOTA-peptides analog to the somatostatin receptors (SSTR) is considered the state of the art to quantify SSTR receptors in vivo [10, 11], while  $^{18}\text{F}$ -fluorodeoxyglucose ( $^{18}\text{F}$ -FDG) PET-CT is used to metabolically characterize more aggressive and higher grade NET lesions [12]. This dual approach has been recently evaluated leading to the development of the NETPET score [13]. Nevertheless, the simple in vivo quantification of receptor expression is not sufficient to characterize the biology of the tumor and the intra-patients and intra-tumor heterogeneity. This drawback might be solved with a better characterization of tumor heterogeneity by the extraction of radiomic features (RFs), as a surrogate biomarker for NET lesions characterization [14], from the  $^{68}\text{Ga}$ -DOTA-peptide PET-CT [15–18]. While scientific interest in radiomics applied to PET imaging is rapidly increasing, the methodological approach needs to be validated and standardized and, thus, harmonization among protocols is needed [19–21]. Indeed, imaging analysis procedures such as tumor segmentation methods, gray-level intensity discretization, and image reconstruction algorithm can affect the RFs [22–25]. Robustness analysis measures the variability of RFs concerning these factors. The identification of robust RFs for  $^{68}\text{Ga}$ -DOTA-TOC PET-CT is fundamental since this innovative modality might be used as a prognostic and predictive tool for evaluating tumor heterogeneity in NET. To our knowledge, there is only one study evaluating the robustness of RFs in function of image acquisition and reconstruction parameters for  $^{68}\text{Ga}$ -DOTA-peptides PET/CT (without considering the consequences of different segmentation approaches) [26], while the extraction of RFs and the assessment of RFs robustness in  $^{18}\text{F}$ -FDG PET/CT imaging has been broadly explored [27–31]. There are several reasons to evaluate the RFs robustness specifically in  $^{68}\text{Ga}$ -DOTA-peptide tracers: a diverse range of positrons compromising the resolution in PET in a different way comparing to  $^{18}\text{F}$ -FDG [32–34]; a different physiological distribution of  $^{68}\text{Ga}$ -DOTA-peptide; and a high inter-patient and intra-patient heterogeneity for both physiological and pathological uptake comparing to  $^{18}\text{F}$ -FDG [35], leading to the necessity to provide different segmentation methods and discretization settings.

The objective of this study was to evaluate the robustness of RFs in function of segmentation methods and discretization settings in  $^{68}\text{Ga}$ -DOTATOC PET/CT images.

## Materials and methods

### Patient selection

270 consecutive patients affected by NET referred to our institution to perform  $^{68}\text{Ga}$ -DOTA-TOC PET/CT between February 2017 and July 2019 were reviewed (IRB protocol: CS2/477). The inclusion criteria of the present study were (1) histologically proven

NET, (2) patients who underwent  $^{68}\text{Ga}$ -DOTA-TOC PET/CT for staging in treatment-naïve patients or restaging after surgery, and (3) willing to sign an informed consent form (ICF). Exclusion criteria were (1) age < 18 years and (2) previous systemic therapies (e.g., somatostatin analogs, chemotherapy, everolimus, and peptide receptor radionuclide therapy). Forty-nine patients with a total of 60 lesions matched the inclusion criteria and were considered in this analysis. Primary tumor sites were GEP-NET, lung NET, and others NET in 77.5% (38/49), 18.4% (9/49), and 4.1% (2/49) of cases, respectively. Patients' characteristics are exposed in detail in Table 1.

### PET/CT acquisition and image reconstruction

All patients underwent PET/CT on an analog 3-dimensional (3D) PET scanner (Philips Gemini Dual-slice EXP scanner—PET Allegro<sup>TM</sup> system with Brilliance CT scanner—Philips Medical Systems, Cleveland, OH). In accordance with the procedural guidelines for PET imaging [36–38], the injected tracer activity was  $145.1 \pm 25.3$  MBq of  $^{68}\text{Ga}$ -DOTA-TOC (range, 100–212 MBq). After 60 min of uptake and following free-breathing CT acquisition for attenuation correction from the vertex of the skull to the

**Table 1** Demographic data and NET characteristics of study subjects (values are given as mean  $\pm$  standard deviation and range)

Demographic data and tumor characteristics			
Characteristic		<i>n</i>	%
<b>Number of patients</b>		49	100%
<b>Sex</b>	Female	22	44.9%
	Male	27	55.1%
<b>Age, years</b> mean $\pm$ sd (range)		61.7 $\pm$ 14.1 (18–83)	
<b>Weight, kg</b> mean $\pm$ sd (range)		76.2 $\pm$ 17.1 (48–115)	
<b>Injected tracer activity, MBq</b> mean $\pm$ sd (range)		145.1 $\pm$ 25.2 (100–212)	
<b>Primary</b>	<b>GEP-NET total</b>	38	77.5%
	Pancreatic	22	57.9%
	Gastro-enteric	16	42.1%
	<b>Lung</b>	9	18.4%
	<b>Other</b>	2	4.1%
<b>NET histological sub-types</b>	G1	33	67.4%
	G2	6	12.2%
	G3	1	2.0%
	Atypical carcinoid	4	8.2%
	Typical carcinoid	5	10.2%
<b>KI67, %</b> mean $\pm$ sd (range)		4.2 $\pm$ 12.9 (1–90)	
<b>Number of lesions</b>	Primary	42	70.0%
	Liver metastasis	8	13.3%
	Bone metastasis	0	0%
	Lymph node metastasis	9	15.0%
	Other metastasis	1	1.7%

mid-thighs (5 mm slice, 40 mAs, and 120 kVp), PET data were acquired in 3-dimensional (3D) mode, covering the same anatomical region of the CT, with 2.5 min per bed position and 6–8 bed positions per patient. The PET scans were reconstructed by ordered subset expectation maximization (OSEM) algorithm (3D-RAMLA), with the following settings: 4 iterations, 8 subsets, and field of view (FOV) of 576 mm. For all reconstructions, matrix size was  $144 \times 144$  voxels, resulting in isotropic voxels of  $4.0 \times 4.0 \times 4.0$  mm<sup>3</sup>. All acquisitions were corrected for photon attenuation (using the corresponding CT image), as well as for scatter and random coincidences.

### Lesion segmentation

For each lesion, a three-dimensional volume of interest (VOI) was manually delineated ( $VOI_m$ ), slice-by-slice, in the OSEM PET images by four independent observers, all nuclear medicine physicians (FC, VL, GP, and BD with 10, 7, 5, and 3 years of expertise, respectively), by using the software LifeX v. 4.81 (IMIV/CEA, Orsay, France—[www.lifexsoft.org](http://www.lifexsoft.org)) [39].

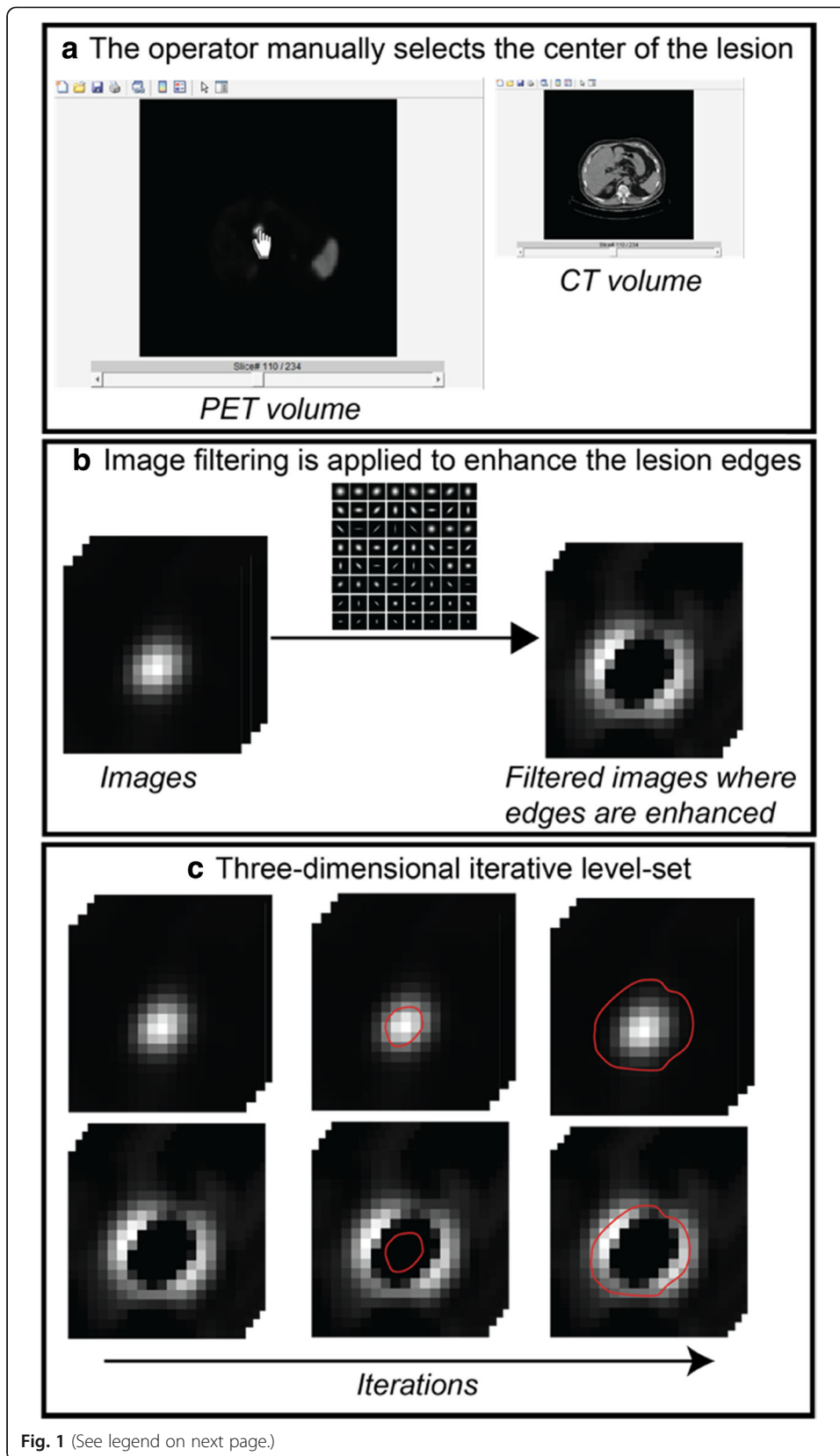
In addition, each lesion was also contoured using a semi-automatic edge-based (SAEB) algorithm ( $VOI_{SAEB}$ ), homemade implemented in MATLAB (MathWorks) code, based on the active contour model proposed by Chan and Vese [40]. The algorithm is semi-automatic since the operator intervention was required in order to insert the central point of the lesion (Fig. 1a). The developed MATLAB graphical user interface allowed the operator to view both the PET and the CT images separately. Edge enhancement filters were applied to emphasize the edges of the lesion (Fig. 1b) and, subsequently, a curve was evolved iteratively on both the original and the edge-enhanced image in order to match the lesion contours by using a level-set formulation (Fig. 1c). The iteration 0 of the level-set, which is the initialization, was the center of the lesion indicated by the operator. The final contour of the lesion ( $VOI_{SAEB}$ ) was achieved at the end of the iterative level-set.

A threshold-based segmentation approach was implemented applying three different thresholds on both manual  $VOI_m$  and  $VOI_{SAEB}$ , defined as 20, 30, and 40% of the  $SUV_{max}$  ( $VOI_{20}$ ,  $VOI_{30}$ , and  $VOI_{40}$ , respectively), as recently suggested by Toriihara et al. [41]. This approach is different from the well-established isocontouring methods frequently used for <sup>18</sup>F-FDG PET/CT, in which the threshold is applied to larger regions of interest containing the tumor [42, 43]. In <sup>68</sup>Ga-DOTA-peptide tracers, the methodology proposed by Toriihara is preferable to exclude surrounding physiological uptake, especially for the segmentation of liver metastases which are very prevalent in metastatic neuroendocrine tumors.

### Intensity discretization

To perform RFs calculation, in particular of textural features, voxels values were redefined considering a limited number of SUV intensity values (gray-level intensity discretization process). To investigate the effect of gray-level discretization, the analysis was performed with two different settings of intensity discretization:

- Absolute resampling with 64 number of gray levels (bins) between 0 and 60 SUV units (“fixed bin size” equal to 0.95, using the IBSI nomenclature [44]), called AR60,



(See figure on previous page.)

**Fig. 1** Semi-automatic edge-based (SAEB) algorithm workflow. The algorithm requires the intervention of an operator to insert the central point of the lesion (**a**) through an interface created in MATLAB, the operator can view both the PET and the CT images separately. As a second step, edge-preserving filters are applied to the image to emphasize the edge of the lesion (**b**) and, after that, and a level-set is used which is a shape that evolves iteratively over the image (**c**). The level-set acts both on the original image of the lesion and on the filtered image in which the contours are highlighted. The iteration 0 of the level set, which would be the initialization, is the center of the lesion indicated by the operator. The final outline of the lesion is achieved at the end of the process

since most of the lesions presented a  $SUV_{max}$  between 0 and 60, as showed in supplemental material (Figure S1A);

- Relative resampling (RR), between minimum and-maximum SUV of the VOI, using a “fixed bin number” equal to 64 number of gray levels (using the IBSI nomenclature [44]) and different sizes of bin, according to the uptake characteristic of each lesion/VOI.

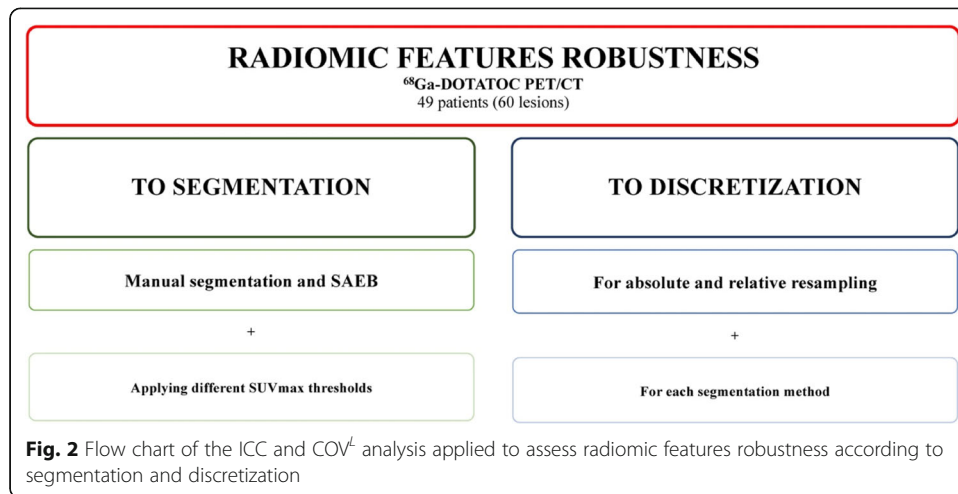
Number of gray levels was set to 64 based on the results of previous studies regarding RFs robustness in  $^{18}F$ -FDG PET/CT [45–47]. The spatial resampling was of  $4 \times 4 \times 4$  mm<sup>3</sup>, according to the resolution limits of the Philips Gemini Dual-slice EXP PET/CT scanner.

### Radiomic features extraction

Radiomics features were extracted from PET images in all the  $VOI_m$  segmented by each nuclear medicine physician, in all the  $VOI_{SAEB}$  and in all the corresponding  $VOI_{20}$ ,  $VOI_{30}$ , and  $VOI_{40}$  using the two intensity rescaling factors (AR60 and RR). Hence, a total of 40 combinations of VOI, threshold, and intensity rescaling factors were tested, as shown in Fig. 2.

A total of fifty-one semi-quantitative PET parameters and RFs were extracted, using LifeX description:

- Ten conventional PET parameters: such as  $SUV_{max}$ ,  $SUV_{mean}$ ,  $SUV_{min}$ ,  $SUV_{peak}$ ,  $SUV_{std}$  SUV quartiles (SUVQ1, SUVQ2, and SUVQ3) and total lesion somatostatin receptor expression (TLSRE);
- Five descriptors of the image intensity histogram: HISTO\_Skewness (asymmetry), HISTO\_Kurtosis (flatness), HISTO\_Energy (uniformity), HISTO\_Entropy\_log2, and \_log10 (randomness);
- Four shape-based features, that describe shape and size of VOI: SHAPE\_Volume (mL), SHAPE\_Volume (voxels), SHAPE\_Sphericity, and SHAPE\_Compacity; and
- Thirty-two textural features: (a) seven features from gray-level co-occurrence matrix (GLCM): describing the correlation between pair of voxels in 13 directions of a three-dimensional space; (b) eleven features from gray-level run length matrix (GLRLM): describing the number and length of run with a certain level of gray in 13 directions of a three-dimensional space; (c) eleven features from gray-level zone length matrix (GLZLM): describing the number and size of zone with a certain level of gray in 13 directions of a three-dimensional



space; (d) three features from neighborhood gray-level different matrix (NGLDM): describing the difference between a voxel and its connected neighbors.

Detailed descriptions of these features can be found in the LifeX documentation ([www.lifexsoft.org](http://www.lifexsoft.org)) [39]. Supplementary Table 1 reports the complete list of computed RFs and the comparison between LifeX and the Imaging Biomarker Standardization Initiative (IBSI) nomenclatures [44]. The GLZLM features of LifeX correspond to gray-level size zone matrix (GLSZM) of IBSI; the two features categories gray-level distance zone matrix (GLDZM) and neighboring gray tone difference matrix (NGTDM) are not measurable in LifeX.

**Statistical analyses**

Quantitative comparisons between VOI<sub>m</sub> and VOI<sub>SAEB</sub> were evaluated through the Dice similarity coefficient (DSC), which measures spatial overlap between two different segmentations of the same lesion:

$$DSC(V_1, V_2) = 2 \frac{|V_1 \cap V_2|}{|V_1| + |V_2|}$$

where |V<sub>1</sub>| and |V<sub>2</sub>| were the volumes of the two segmentations to be compared, |V<sub>1</sub> ∩ V<sub>2</sub>| was the volume of the overlap between V<sub>1</sub> and V<sub>2</sub>. DSC values can range from 0, when the two segmentations have no overlap, to 1 when the two segmentations are coincident [42].

The algorithm for simultaneous truth and performance level estimation (STAPLE), which takes a collection of segmentations of an image and computes a probabilistic estimate of the true segmentation [48], was also used to compare VOI<sub>SAEB</sub> with the “true” segmentation (VOI<sub>STAPLE</sub>) derived by the four VOI<sub>m</sub>.

Robustness of RFs was assessed by two-way mixed effects intra-class correlation coefficients (ICC) to evaluate consistency and coefficient of variance for each lesion (COV<sup>L</sup>) to evaluate agreement in the various settings.

The intra-class correlation coefficients (ICC) was defined as:

$$\text{ICC} = \frac{\text{BMS} - \text{RMS}}{\text{BMS} + (N - 1) \times \text{RMS}}$$

where BMS is the between-subjects mean square, RMS is the residual mean square and  $N$  is the number of measurements of the RF (e.g., 2 in the case of intensity discretization, being AR60 and RR). RFs were considered highly robust in case of  $\text{ICC} > 0.9$ , robust if  $\text{ICC} > 0.8$ , moderately robust if ICC was between 0.5 and 0.8 and poorly robust if ICC was  $< 0.5$  [25, 49, 50].

The coefficient of variation ( $\text{COV}^L$ ), which is commonly used to measure relative dispersion, calculated for each lesion ( $L$ ) was defined as:

$$\text{COV}^L = 100 \times \frac{\sqrt{\frac{1}{N-1} \sum_{k=1}^N (m_k^L - \underline{m}^L)^2}}{\underline{m}^L}$$

where  $m_k^L$  is the measurement of RFs for lesion  $L$  for a specific segmentation and intensity discretization ( $k$ ) and  $\underline{m}^L$  is the mean value of lesion  $L$  over the considered combinations of segmentation and discretization approaches, as presented in the study of Bailly et al. [26]. RFs with low percentage of  $\text{COV}^L$  are characterized by low dispersion, on contrary RFs with high percentage of  $\text{COV}^L$  are characterized by high dispersion.

To investigate the relationship between RFs and lesion volume and  $\text{SUV}_{\max}$ , a Pearson's correlation analysis was carried out. To consider a unique RF value for every segmentation, RFs values were averaged across segmentations.

All analyses were performed using statistical R software (R Foundation, Vienna, Austria [51]).

## Results

### Quantitative comparison of manual and SAEB segmentation

Mean value of DSC comparing  $\text{VOI}_{\text{SAEB}}$  with  $\text{VOI}_{\text{STAPLE}}$  was  $0.75 \pm 0.11$  (0.45–0.92), while mean value of DSC among  $\text{VOI}_m$  was  $0.78 \pm 0.03$  (0.75–0.83). Examples of segmentation performed by SAEB and operators for three different lesions are shown in Fig. 3. DSC boxplots between  $\text{VOI}_{\text{SAEB}}$  and the different  $\text{VOI}_m$  and between manual operators for each lesion are reported in Fig. 4a, b.

Comparison between operators showed a perfect segmentation overlap ( $\text{DSC} = 1$ ) for 24 out of 60 lesions, applying the 40%  $\text{SUV}_{\max}$  threshold; mean DSC using different  $\text{SUV}_{\max}$  threshold are reported in Fig. 4c.

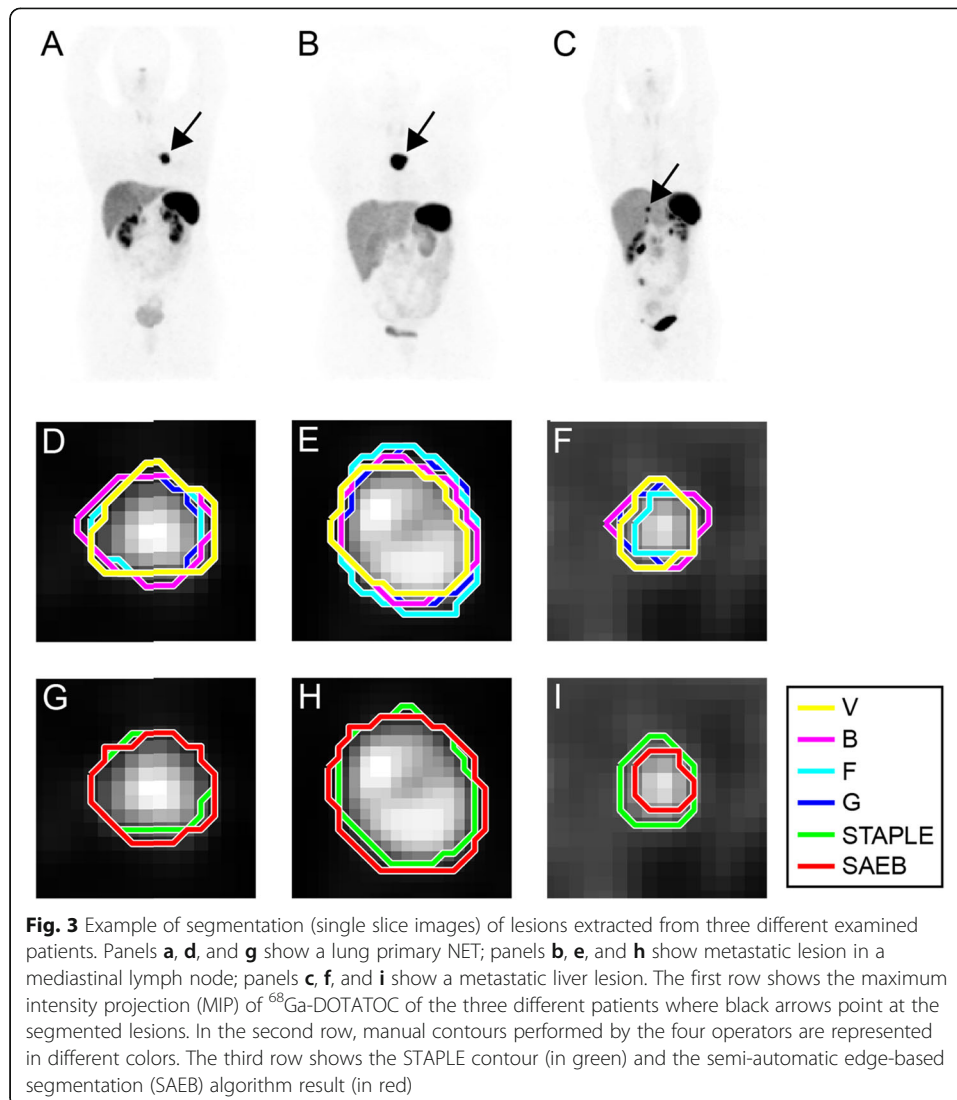
Mean DSC values improved as the  $\text{SUV}_{\max}$  threshold applied increases. The volume distributions for different thresholds are shown in supplementary material (Figure S1B).

### Impact of different segmentation approaches on RF

Using no threshold and applying AR60 intensity rescale factors, 64.7% of RFs showed high robustness ( $\text{ICC} > 0.9$ ) to segmentation (7/10 conventional, 3/6 histogram, 2/4 shape, and 21/31 textural) (Fig. 5a).

Using a 40%  $\text{SUV}_{\max}$  threshold, the robustness of RFs to segmentation ( $\text{ICC} > 0.9$ ) increased to 86.5% of RFs. An increase of the  $\text{SUV}_{\max}$  threshold produced a substantial increase of ICC of the following features: CONV\_SUVmin, CONV\_SUVQ1, CONV\_SUVQ2, SHAPE\_Sphericity, SHAPE\_Compacity, GLCM\_Correlation, NGLDM\_

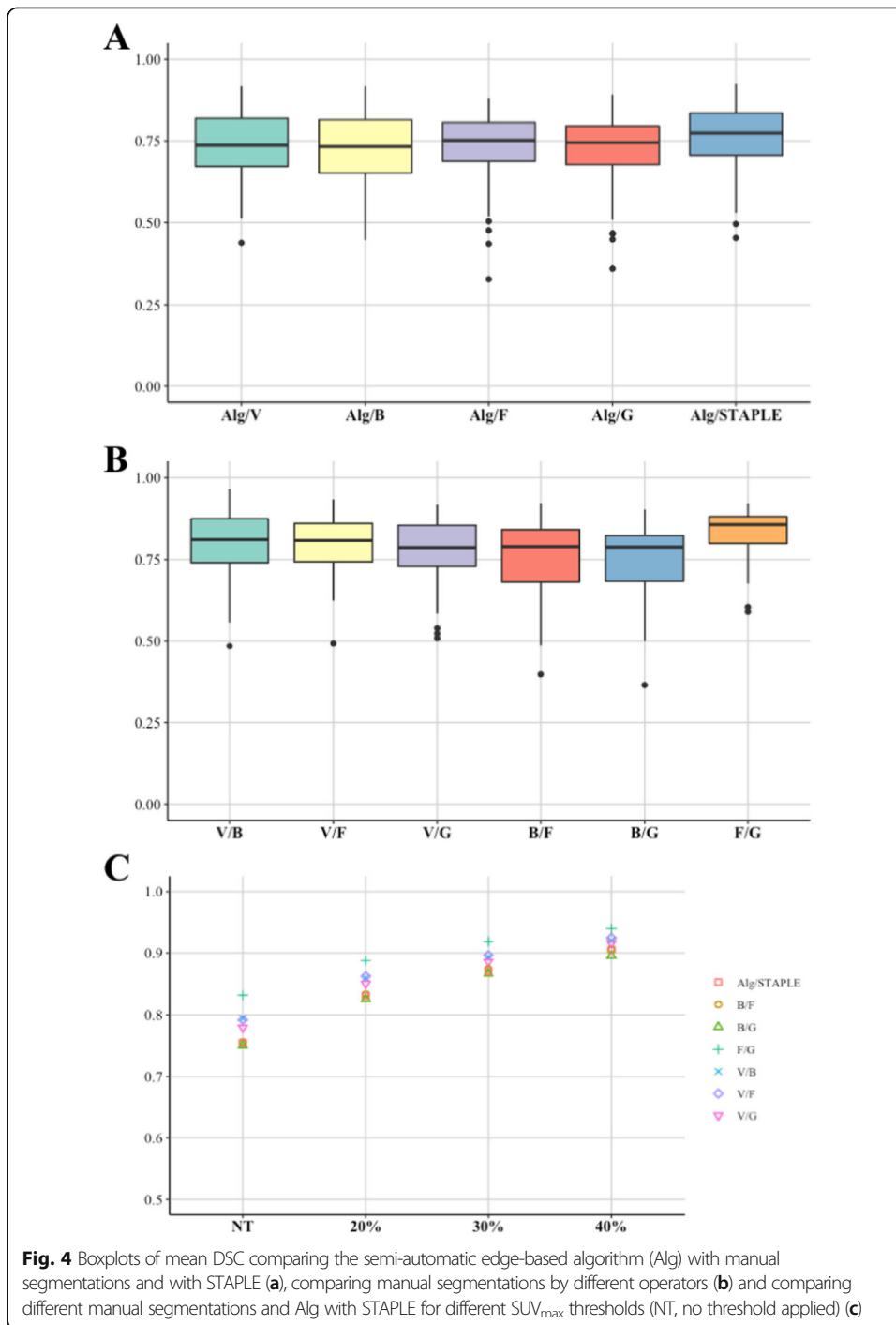




Contrast, NGLDM\_Busyness, GLZLM\_LZE, GLZLM\_LZLGE, GLZLM\_LZHGE, and GLZLM\_ZP while lower increase was observed for the rest of features (Fig. 5a). Further, using a 40%  $\text{SUV}_{\max}$  threshold, textural features were not computed in 22 lesions due to low number of voxels.

About the corresponding  $\text{COV}^L$  analysis, when no threshold was applied, the grade of dispersion of the majority of RFs was rather low: median  $\text{COV}^L$  values were below 10% for 47% of RFs and below 20% for 75% of RFs (Fig. 5b). Only two RFs (GLZLM\_LZE and GLZLM\_LZLGE) showed a  $\text{COV}^L > 50\%$ . Using a 40%  $\text{SUV}_{\max}$  threshold, median values of  $\text{COV}^L$  were lower than 10% for all the RFs (Fig. 5c).

ICC and  $\text{COV}^L$  analysis regarding robustness to  $\text{SUV}_{\max}$  thresholds (no threshold, 20%, 30%, 40%) using AR60 are shown in the supplemental material (Figure S2). 50.9% of RFs (5/10 conventional, 3/6 histogram, 0/4 shape and 18/31 textural) showed high robustness ( $\text{ICC} > 0.9$ ). The results of  $\text{COV}^L$  showed a high variability of the majority of RFs in function of different  $\text{SUV}_{\max}$  thresholds. Median value of  $\text{COV}^L$  was  $< 10\%$  for few RFs, namely  $\text{SUV}_{\max}$ ,  $\text{SUV}_{\text{peak}}$  (0.5 ml and 1 ml), HISTO\_Entropy (log10 and



log2), GLCM\_Homogeneity, GLCM\_Contrast, GLCM\_Entropy (log10 and log2), GLCM\_Dissimilarity, GLRLM\_SRE, GLRLM\_LRE, GLRLM\_RP, GLZLM\_SZE, and GLZM\_ZP.

**Impact of different discretization settings on RFs**

Comparing the five VOI delineations (4  $VOI_m$  and  $VOI_{SAEB}$ ) and applying no  $SUV_{max}$  threshold (Fig. 6a), median value of ICC for the two intensity discretization approaches

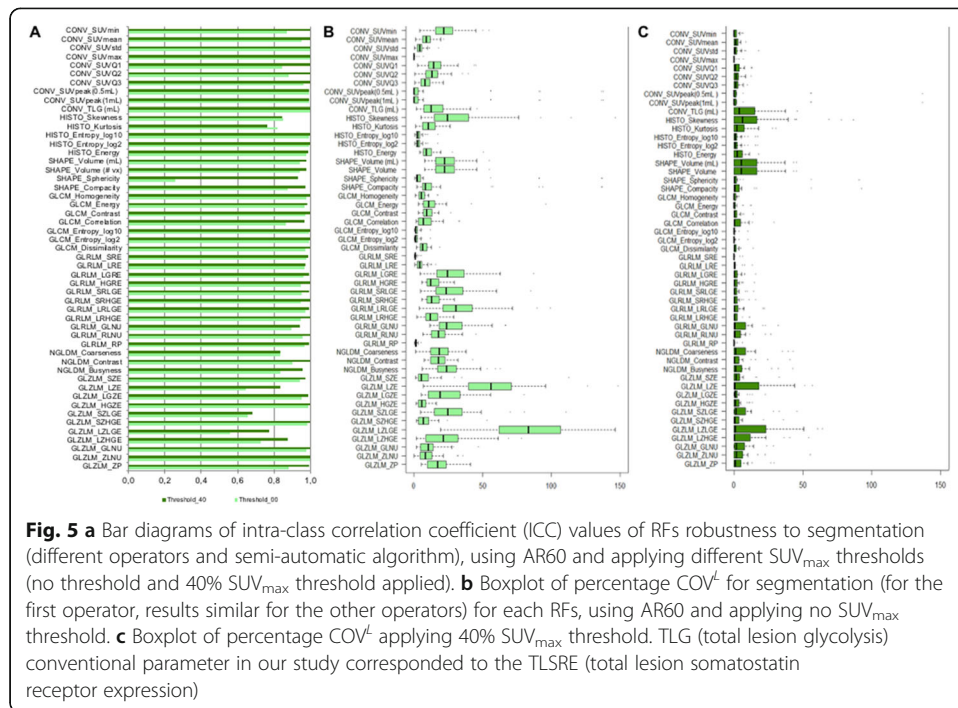


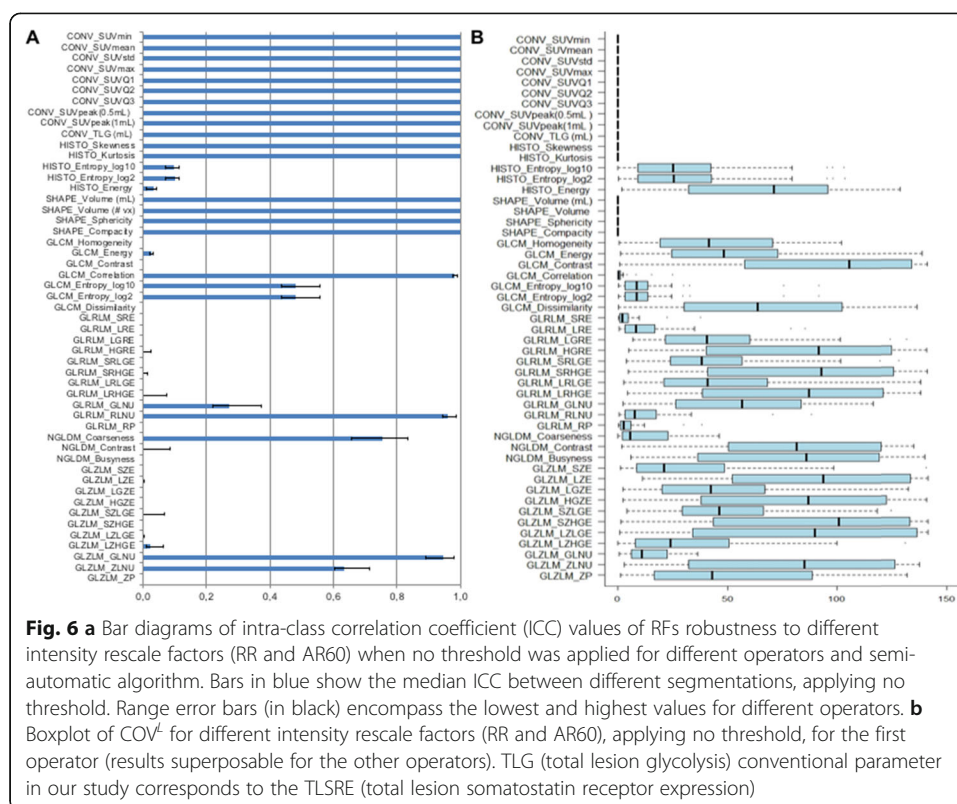
**Fig. 5** a Bar diagrams of intra-class correlation coefficient (ICC) values of RFs robustness to segmentation (different operators and semi-automatic algorithm), using AR60 and applying different  $SUV_{max}$  thresholds (no threshold and 40%  $SUV_{max}$  threshold applied). b Boxplot of percentage  $COV^L$  for segmentation (for the first operator, results similar for the other operators) for each RFs, using AR60 and applying no  $SUV_{max}$  threshold. c Boxplot of percentage  $COV^L$  applying 40%  $SUV_{max}$  threshold. TLG (total lesion glycolysis) conventional parameter in our study corresponded to the TLSRE (total lesion somatostatin receptor expression)

(AR60 and RR) was equal to 1 for all conventional and shape features, HISTO\_Skewness and HISTO\_Kurtosis (not affected by the discretization), and for only three textural features, namely GLCM\_Correlation, GLRLM\_RLNU, and GLZLM\_GLNU. Overall, the percentage of highly robust features was 37% (10/10 conventional, 2/5 histogram, 4/4 shape, and 3/32 textural). The majority of the remaining textural features showed very poor robustness to discretization settings except for NGLDM\_Coarseness which had a median ICC > 0.7. The  $COV^L$  analysis (Fig. 6b) highlighted in general low  $COV^L$  values for all the RFs with high ICC (conventional, shape, HISTO\_Skewness and HISTO\_Kurtosis, GLCM\_Correlation, GLRLM\_RLNU, and GLZLM\_GLNU). The majority of the other textural features were characterized by a very high dispersion, corresponding to a high percentage of  $COV^L$  value. Only GLCM\_Entropy (log10 and log2), GLRLM\_SRE, GLRLM\_LRE, GLRLM\_RP presented a  $COV^L < 10\%$ , despite a corresponding low ICC for these RFs.

**RFs correlation with  $SUV_{max}$  and volume**

Pearson correlation coefficients of RFs with volume (for AR60, without  $SUV_{max}$  threshold and with 40%  $SUV_{max}$  threshold applied, respectively) and with  $SUV_{max}$  of the ROI (AR60 and RR, no threshold applied) are shown in Fig. 7.

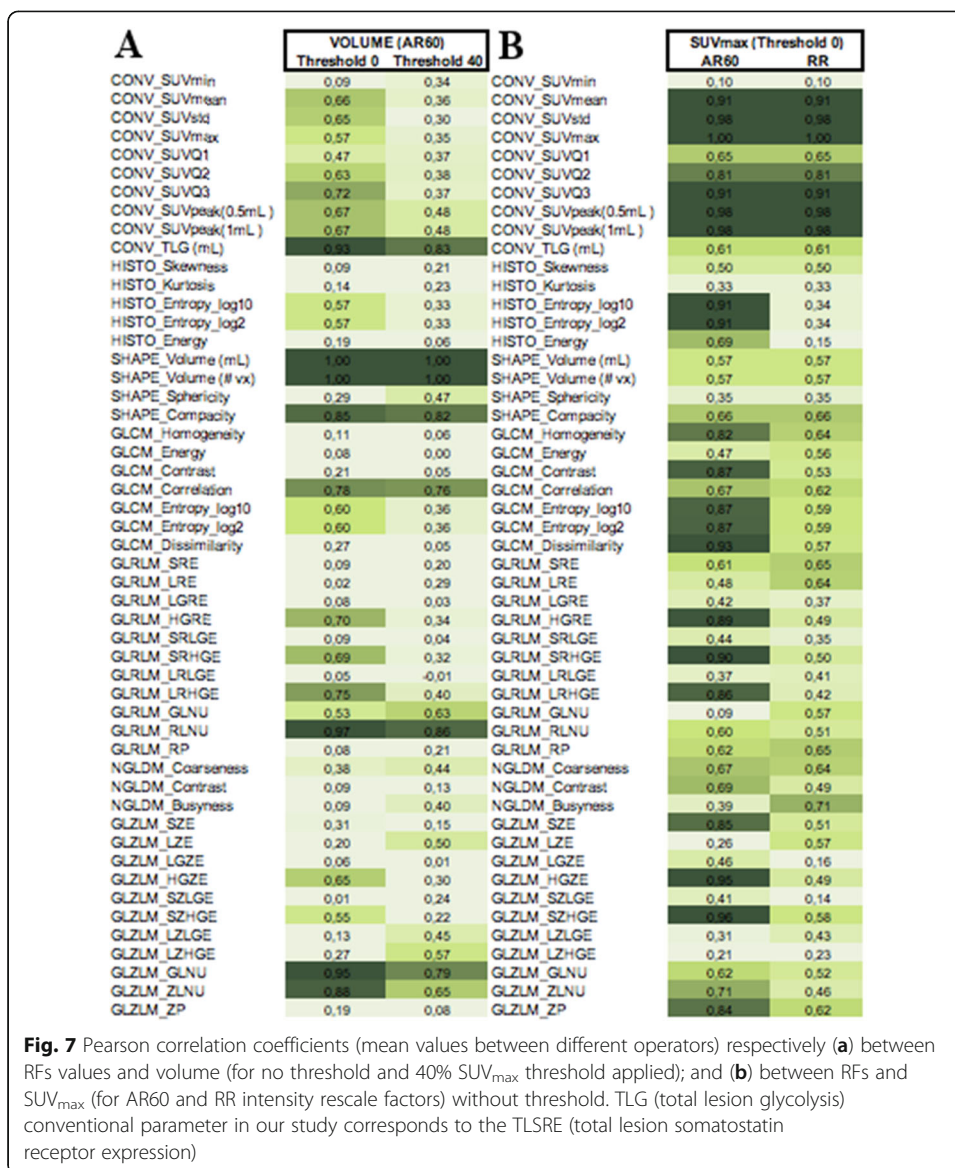
The following RFs showed high correlation ( $r > 0.9$ ) with volume, regardless of  $SUV_{max}$  threshold: TLSRE, SHAPE\_Compacity, GLRLM\_RLNU, and GLZLM\_GLNU. Regarding correlation with  $SUV_{max}$ , the following RFs showed very high correlation ( $r > 0.9$ ) when AR60 was employed: HISTO\_Entropy (both\_log10 and\_log2), GLCM\_Dissimilarity, GLRLM\_SRHGE, GLZLM\_HGZE, and GLZLM\_SZHGE. When RR was used, no RFs were highly correlated with  $SUV_{max}$  (except for most part of conventional SUV features).



## Discussion

Our study sought to identify robust RFs in  $^{68}\text{Ga}$ -DOTA-TOC PET/CT, as a result of different segmentation and gray-level intensity discretization methods of the images. The major findings of our study were the following: (a) 64.7% of RFs (7/10 conventional, 3/6 histogram, 2/4 shape, and 21/31 textural) showed high robustness in terms of consistency (ICC > 0.9) and agreement (low median  $COV^L$  value) to different operators without  $SUV_{\max}$  threshold applied (manual segmentation); (b) increasing the  $SUV_{\max}$  isocontouring threshold had a positive effect on RFs robustness to segmentation. However, this approach might lead to a loss of important biological information on the population studied and reduction of analyzable lesions with textural features due to low number of voxels; (c) quantitative comparison between a semi-automatic edge-based (SAEB) algorithm and manual segmentation showed a dice similarity coefficient (DSC) of  $0.75 \pm 0.11$  comparable to DSC between operators ( $0.78 \pm 0.03$ ). These results suggest that a semi-automatic algorithm might be able to aid expert segmentation to reduce operator variability and analysis time [36, 42]; (d) the use of absolute intensity rescaling factor (AR60) achieved higher robustness of RFs to segmentation than relative (RR) intensity rescaling factor.

In monocentric studies, image segmentation is one of the first step to take into account in radiomic analysis, since it is a possible source of RFs variability. Overall, RFs robustness to segmentation resulted to be quite good applying no  $SUV_{\max}$  threshold (ICC > 0.9 for 64.7% RFs), using AR60 intensity discretization method (Fig. 5a). Only one morphological feature, SHAPE\_Sphericity, resulted not robust to segmentation. However, its ICC value was furtherly decreased from Lifex software due to an assigned



artificial feature value equal to zero for VOIs smaller than 64 voxels rather than a *Not A Number* (NaN) as other RFs. This occurred also for SHAPE\_Compacity for a total of 7 lesions and only for some operator, leading to a high inter-operator variability. After removing these lesions, the ICC increased for both SHAPE\_Sphericity (from ICC = 0.27 to ICC = 0.59) and SHAPE\_Compacity (from ICC = 0.88 to ICC = 0.95).

In line with previous studies [52, 53], GLZLM (also called GLSZM) features and in particular the ones measuring zones with low gray-level (SZLGE and LZLGE) resulted to have a moderate robustness (ICC from 0.5 to 0.8) to segmentation (Fig. 5a). This is likely related to the lower uptake in lesions edges, where operators and SAEB segmentation showed a higher variability (Fig. 3).

When using AR60 intensity discretization method, the SUV<sub>max</sub> thresholding had a considerable impact on inter-segmentation ICC values of conventional, shape, and GLRLM features (Fig. 5a). At the same time, however, it is clear that the SUV<sub>max</sub> thresholding has an important impact on the dispersion (agreement) of RFs, reducing it

significantly, with a progressive flattening of all RFs  $COV^L$  values toward zero (Fig. 5b, c). These results lead to considering segmentation with a 40%  $SUV_{max}$  threshold as preferable from the point of view of robustness, increasing the similarity between segmentations (Fig. 4c). However, its use may lead to a significant loss of relevant information for diagnosis and prognosis. These findings are in accordance with previous studies, reporting that segmentation with 40%  $SUV_{max}$  threshold yields superior inter-observer reproducibility of texture features in  $^{18}F$ -FDG PET/CT images, despite the loss of information about tumor heterogeneity related to exclusion of voxel intensities below the fixed 40% threshold, such as those arising from low-activity tumor regions or tumor boundaries. However, as early demonstrated by the study of Biehl et al in  $^{18}F$ -FDG PET/CT images [54], there is no consensus in the use of  $SUV_{max}$  threshold, because this parameter can lead to an over- and/or underestimation of lesion PET volume compared with CT volume related to low resolution, inherent noise, high uncertainties in lesion boundaries, and motion blurring of the lesion related to the tomography characteristics [42]. Further, from a technical point of view, the use of high  $SUV_{max}$  threshold could reduce number of voxels of the VOI denying computation of textural features. In our opinion, the concern related to the use of threshold-based segmentation methods in  $^{68}Ga$ -DOTA-peptide PET-CT images must be even higher due to the aforementioned heterogeneity of somatostatin receptors expression in neuroendocrine tumors which may explain that currently the few studies of radiomics with  $^{68}Ga$ -DOTA-peptide in the literature has been made on a manual-based segmentation [55–58].

Image gradient showed to be useful for tumor segmentation in  $^{18}F$ -FDG PET/CT images, as highlighted by Pfeahler et al. [59] and Foster et al. [42]. In this study, we demonstrated the suitability and added value of using an automatic image gradient segmentation in  $^{68}Ga$ -DOTA-peptide PET images, given the high SUV variability and the presence of high SUV values for normal tissues. For these reasons, we believe that automatic and semi-automatic segmentation methods are crucial for the radiomics analysis of NET in  $^{68}Ga$ -DOTA-peptide images.

Our results regarding tumor segmentation accuracy are promising since DSC comparing the SAEB segmentation with the manual segmentations was  $0.75 \pm 0.11$  (median 0.77). The SAEB algorithm is characterized by its hybrid nature: the curve evolves in the image looking to both the original image (important for homogeneity) and the edge-enhanced image (important for discontinuities detection). This feature allows the SAEB algorithm to behave reproducibly within lesions in different locations, with different image appearances and different background uptakes, such as blob-like lesions with dark background (Fig. 3a, d and g), heterogeneous lesions (Fig. 3b, e, and h) and liver lesions where background present SUV values comparable to the lesion (Fig. 3c, f, and i). Thus, the use of automatic and semi-automatic segmentation methods, such as SAEB algorithm, appears to be crucial in future studies assessing robustness or clinical significance of RFs in  $^{68}Ga$ -DOTA SSTR-peptide PET/CT imaging, in order to reduce inter- and intra-reader variability of manual segmentation methods, which is also time-consuming [42, 44], and in order to reduce relevant information loss secondary to the application of 40%  $SUV_{max}$  threshold. However, further studies are needed to validate our semi-automatic segmentation methods (SAEB).

Another interesting result of our study is related to the negative impact of the relative resampling intensity discretization (which corresponded to the fixed bin number) on the robustness to segmentation of the majority of textural features analyzed. As the rescaling is carried out according to the minimum and maximum values of the VOI, the same image is rescaled differently depending on the segmentation operator/method used, leading to high variability also in RFs values. Recently, Zwanenburg et al. [20] highlighted that, as both discretization methods have their particular advantages and disadvantages, they should not be treated as equivalent. Hence, an image biomarker should be considered different to consist of the discretization method and level, in addition to its scale and base feature definition.

Anyway, the use of relative resampling is not recommended in PET images, as already observed in  $^{18}\text{F}$ -FDG PET/CT [45–47]. At least in clinical cases, the “fixed bin number” is intuitively less appropriate: it is based on the range of SUV intensities found in the volume of interest, with low SUVs corresponding to low bin numbers and high SUVs corresponding to high bin numbers; hence bin width (in SUV) and SUV range may vary between images in a cohort, even though the number of bins is consistent [20]. For the identification of RFs as new cancer-specific biomarker (e.g., NET), it is important that the textural features values would, be directly comparable, both inter- and intra-patient, in order to derive meaningful conclusions. Moreover, NETs are characterized by an extremely variable expression of somatostatin receptors in  $^{68}\text{Ga}$ -DOTA-peptides with a corresponding broader range for SUV values (from close to 0 up to higher than 100) compared to  $^{18}\text{F}$ -FDG PET/CT, causing a greater impact of the RR in the final discretized uptake values. This concept has been already emphasized by several studies: beyond all the variabilities related to the tomographs, segmentations, and post-processing settings, the robustness of RFs is also related to the tumor characteristic and behavior [52, 60–62] and to the radiotracer analyzed, as recently demonstrated by Lu et al. [63] that studied the stability of RFs for nasopharyngeal carcinoma on both  $^{11}\text{C}$ -choline and  $^{18}\text{F}$ -FDG PET/CT images, with different results. In accordance with previous studies [20, 25], the impact of intensity discretization on textural features was stronger than segmentation. This is exactly the case of textural features, where differentiation between high and low-gray levels is needed, and thus, the choice of the discretization setting is relevant. When using no  $\text{SUV}_{\text{max}}$  threshold, only four textural features resulted to be consistent: GLCM\_Correlation, GLRLM\_RLNU, NGLDM\_Coarseness, and GLZLM\_GLNU (Fig. 6).

ICC and  $\text{COV}^L$  provided in general similar information. Generally, we reported low ICC and high  $\text{COV}^L$  or the opposite. Anyway, there were also RFs with low consistency (low ICC) and high agreement (low  $\text{COV}^L$ ) or high consistency (high ICC) and low agreement (high  $\text{COV}^L$ ). Representative examples were GLCM\_Entropy (both  $_{\log 10}$  and  $_{\log 2}$ ), GLRLM\_SRE, GLRLM\_LRE, and GLRLM\_RP which had low consistency but good agreement ( $\text{COV}^L < 10\%$ ) to discretization. For these RFs, although measurements were not correlated when changing intensity discretization methods, the relative percentage of deviation was low (Figure S3). On the other hand, when evaluating robustness to  $\text{SUV}_{\text{max}}$  threshold, ICC was sometimes high even if  $\text{COV}^L$  was also high because, despite the great variability, the RFs remained correlated by changing the parameters, as we can observe in particular for GLRLM\_LGRE, GLRLM\_SRLGE, GLRLM\_LRLGE, and GLZLM\_LZLGE for the threshold variability (Fig. 6 and Figure S4).

This behavior was due to the very small, close to zero, values of these RFs, which produced high  $COV^L$  values. Our study highlights the importance of the discretization settings chosen due to its high impact on the RFs robustness, which seems even higher in  $^{68}\text{Ga}$ -DOTA-peptide comparing to  $^{18}\text{F}$ -FDG PET/CT images (due to the widest range of SUV values in  $^{68}\text{Ga}$ -DOTA-peptide images in NET). However, discretization is a controllable variable, while segmentations do not. Respect of segmentation, there are essentially three categories of features: a first group of features almost not sensitive to segmentation with high ICC and low  $COV^L$  values (e.g. SUVmean, figure S5 a), a second group of features with high ICC with relative high  $COV^L$  values (e.g., TLG, figure S5 b) and a third group with low ICC and high  $COV^L$  values (e.g., GLZLM\_SZLGE, figure S5 c), that could probably be useless in the absence of a universally standardized and totally automatic segmentation method.

Finally, regarding Pearson's correlation between RFs and  $SUV_{\max}$  and volume, most of the RFs extracted showed a poor correlation with volume. Only two textural features had a strong correlation (coefficient values  $>0.8$  or  $<-0.8$ ) with the volume, for all thresholds and discretization (GLRM\_RLNU and GLZLM\_GLNU). Regarding the correlation with  $SUV_{\max}$ , no features showed a strong correlation for all thresholds and discretization. These results suggest that RFs could provide additional information to better characterize NETs, regardless of volume and SUV parameters.

The extraction of robust RFs from  $^{68}\text{Ga}$ -DOTA SSTR-peptide PET/CT might contribute to solve some limitations related to the clinical evaluation of the SSTR expression in NET. At present, no consensus has been already reached regarding the assessment of patients who need to be investigated with both  $^{18}\text{F}$ -FDG and  $^{68}\text{Ga}$ -DOTA-peptide PET/CT (even if it is more probable that NET neoplasms with Ki67  $>15\%$  will have positive lesions in  $^{18}\text{F}$ -FDG PET/CT [64, 65]). Furthermore, an early detection of more aggressive disease with  $^{18}\text{F}$ -FDG PET/CT does not necessarily reflect a change in the therapeutic strategy. Finally, conventional semi-quantitative PET parameters showed a sub-optimal feasibility to select patients for receptor radionuclide therapy (PRRT) and to evaluate response to PRRT. In this scenario, the quantitative analysis offered by radiomics might be applied as prognostic biomarker and predictor of tumor heterogeneity in NET.

### Limitation

This study is not exempt from limitations. First, we did not initially perform a phantom study. To overcome this limitation, as recommended in the radiomics quality score (RQS) proposed by Lambin et al. [66], we are currently adapting our methodology for a study on an anthropomorphic phantom filled with synthetic lesions as obtained from PET/CT images and created by the 3D printer. This model will reflect realistic tumor shapes and heterogeneity uptakes for a prospective evaluation of RFs robustness. Second, we limited our analysis to the RFs provided by the LIFEx software. Even if LIFEx's RFs are the most representative ones, they are only a limited set of the biggest group of RFs provided by the IBSI nomenclature, furthermore, two IBSI categories are not included; further and more comprehensive studies on this aspect are needed. Third, NET are rare tumors and G3 NET and G3 NEC are rarely evaluated with  $^{68}\text{Ga}$ -DOTA SSTR-peptide; for this reason, our sample size is yet too small and heterogeneous (as



shown in Table 1) to evaluate the possible correlation between robust RFs with the histological NET grading system. The phantom study will lead to the possibility to enrolled NET patients from different centers, solving also limitations regarding sample size. Fourth, the difficulty of edge-based algorithms in the segmentation of lesions with a similar uptake background or with small ( $< 16 \text{ cm}^3$ ) or large dimension ( $> 160 \text{ cm}^3$ ) [50] has been previously highlighted. However, we acknowledge that the number of cases analyzed in this study is not enough to quantitatively validate the algorithm in the aforementioned conditions. Nevertheless, these results encouraged us to start evaluating also this on the 3D-printer based phantom study aimed to assess the performance of SAEB analyzing both spherical lesions, non-uniform and non-spherical volumes with different sizes and different backgrounds, reproducing the human-like lesions [60, 67].

## Conclusion

Our results suggest that the use of RFs is feasible also in  $^{68}\text{Ga}$ -DOTA-TOC PET/CT. The manual delineation of VOI had an impact on RFs values dependent on RF type, preserving the correlation with high ICC values in most cases despite some relatively high  $\text{COV}^L$  values. The 40%  $\text{SUV}_{\text{max}}$  threshold increased the RFs robustness, but with a potential loss of information and analyzable lesions. Finally, the gray-level discretization influences the robustness of RFs, which vary depending on the use of relative or absolute resampling. In our opinion, an absolute resampling better suited to the evaluation of NETs with functional imaging ( $^{68}\text{Ga}$ -DOTA-TOC PET/CT).

These results suggest the needing to standardize the methodology used in the radiomic PET studies in  $^{68}\text{Ga}$ -DOTA-TOC PET/CT. Moreover, a semi-automatic segmentation algorithm might be helpful to solve both the impact of different manual segmentations on RFs robustness and the loss of valuable information due to  $\text{SUV}_{\text{max}}$  threshold segmentation method.

## Supplementary Information

The online version contains supplementary material available at <https://doi.org/10.1186/s40658-021-00367-6>.

**Additional file 1: Table S1.** LifeX radiomic features description according to the Imaging Biomarker Standardization Initiative (IBSI) description (update 17 December 2019). LifeX version was 4.81. **Figure S1.** Box plots showing the distribution of  $\text{SUV}_{\text{max}}$  (panel A) and Volume (panel B). **Figure S2.** (A) Bar diagrams of intra-class correlation coefficient (ICC) values of RFs for robustness to  $\text{SUV}_{\text{max}}$  thresholding. Bars show the median ICC between the different segmentations for the absolute intensity rescale factor AR60. Range error bars (in black) encompass the lowest and highest values for different operators. (B) Boxplot of  $\text{COV}^L$  for different threshold (20, 30, 40%) for each RFs, for the first operator (results superposable for the other operators). TLG (total lesion glycolysis) conventional parameter in our study corresponds to the TLSRE (total lesion somatostatin receptor expression). **Figure S3.** Radiomic features with moderate or poor consistency ( $\text{ICC} < 0.80$ ), but high agreement (median  $\text{COV}^L < 10\%$ ) to intensity discretization. The RFs were:  $\text{GLCM\_Entropy\_log2}$ ,  $\text{GLCM\_Entropy\_log10}$  (not shown),  $\text{GLRLM\_SRE}$ ,  $\text{GLRLM\_LRE}$  and  $\text{GLRLM\_RP}$ . Value of the RFs for each lesion are presented in the top row; boxplots of  $\text{COV}^L$  for the first operator are presented in the bottom row. **Figure S4.** Radiomic features with high consistency ( $\text{ICC} > 0.90$ ), but low agreement (median  $\text{COV}^L > 10\%$ ) to  $\text{SUV}_{\text{max}}$  thresholds (0, 20, 30 and 40%). The RFs were:  $\text{GLRLM\_LGRE}$ ,  $\text{GLRLM\_SRLGE}$ ,  $\text{GLZLM\_LGZE}$  and  $\text{GLZLM\_LZLGE}$ . Value of the RFs for each lesion are presented in the top row; boxplots of  $\text{COV}^L$  for the first operator are presented in the bottom row. **Figure S5.** Boxplot showing the distribution of RF value for each operator. The three RFs chosen are the most representative of the impact of segmentation on ICC. Segmentation did not affect  $\text{SUV}_{\text{mean}}$  (A) and TLG (B) in terms of ICC, although TLG was characterized by not negligible dispersion (percentage of  $\text{COV}^L$ ) in our study. In contrast, segmentation had a high impact on  $\text{GLZLM\_SZLGE}$  (C) in terms of both ICC and  $\text{COV}^L$ . Mean  $\text{COV}^L$  of  $\text{SUV}_{\text{mean}}$ , TLG and  $\text{GLZLM\_SZLGE}$  was  $8.33 \pm 3.96$ ,  $13.38 \pm 8.52$  and  $30.67 \pm 27.29$ , respectively.

## Abbreviations

$^{18}\text{F}$ -FDG:  $^{18}\text{F}$ -fluorodeoxyglucose; CT: Computed tomography; FOV: Field of view; GLCM: Gray-level co-occurrence matrix; GLNUr: Gray-level non-uniformity for run; GLNUz: Gray-level non-uniformity for zone; GLRLM: Gray-level run length matrix; GLZLM: Gray-level zone length matrix; HGRE: High gray-level run emphasis; HGZE: High gray-level zone

emphasis; IBSI: Imaging biomarker standardization initiative; ICH – GCP: International Conference on Harmonization - Good Clinical Practice; LGRE: Low gray-level run emphasis; LGZE: Low gray-level zone emphasis; LRE: Long-run emphasis; LRHGE: Long-run high gray-level emphasis; LRLGE: Long-run low gray-level emphasis; LZE: Long-zone emphasis; LZHGE: Long-zone high gray-level emphasis; LZLGE: Long-zone low gray-level emphasis; MIP: Maximum intensity projection; MTV: Metabolic tumor volume; NET: Neuroendocrine tumor; NGLDM: Neighborhood gray-level different matrix; OSEM: Ordered subset expectation maximization; PET: Positron emission tomography; RF: Radiomic features; RLNU: Run length non-uniformity; ROI: Region of interest; RP: Run percentage; SAEB: Semi-automatic edge-based; SRE: Short-run emphasis; SRHGE: Short-run high gray-level emphasis; SRLGE: Short-run low gray-level emphasis; SSTR: Somatostatin receptor; SZE: Short-zone emphasis; SZHGE: Short-zone high gray-level emphasis; SZLGE: Short-zone low gray-level emphasis; SUV: Standardized uptake value; TLSRE: Total lesion somatostatin receptor expression; VOI: Volume of interest; ZLNU: Zone length non-uniformity; ZP: Zone percentage

### Acknowledgements

We would like to express our gratitude to the anonymous patients on whom this work is based and the staff of the Division of Nuclear Medicine for their excellent technical support.

### Authors' contributions

DD, FM, VL, BDS, and OR designed the study; VL collect the data; VL, BD, FC, and GP performed the manual segmentation; BDS and FM create the MATLAB homemade code for the semi-automatic algorithm; VL, BDS, OR, and EG conducted the statistical analysis; PT, FC, FM, and DD contributed in the review of the data and the statistical analysis; VL and BDS wrote the manuscript; all the authors discussed the results and commented on the manuscript. All authors approved the final manuscript.

### Funding

Nuclear Medicine of A.O.U. Città della Salute e della Scienza di Torino, University of Turin, is supported by a grant from CRT Foundation (*Fondazione Cassa di Risparmio di Torino*) for the project "Radiomics in the Study of Neuroendocrine Tumors in Nuclear Medicine: Innovative Method for the Study of Tumor Heterogeneity". No further specific grants from funding agencies in the public, commercial, or not-for-profit sectors were received for this study.

### Availability of data and materials

The datasets used and/or analyzed during the current study are available from the corresponding author on reasonable request.

### Ethics approval and consent to participate

This is a retrospective, observational study approved by the ethical committee A.O.U. Città della Salute e della Scienza di Torino (IRB protocol: CS2/477) and only patients with documented willingness to the use of their medical data for research were included.

### Consent for publication

Not applicable

### Competing interests

The authors declare that they have no competing interests in relation to the present study.

### Author details

<sup>1</sup>Nuclear Medicine Unit, Department of Medical Sciences, University of Turin, Corso Dogliotti 14, 10126 Turin, Italy. <sup>2</sup>Biolab, Department of Electronics and Telecommunications, Politecnico di Torino, Turin, Italy. <sup>3</sup>Medical Physics Unit, AOU Città della Salute e della Scienza, Turin, Italy. <sup>4</sup>Department of Endocrinology, University Hospital of Brest, Politecnico di Torino Brest, Turin, France.

Received: 8 July 2020 Accepted: 9 February 2021

Published online: 27 February 2021

### References

- Oronsky B, Ma PC, Morgensztern D, Carter CA. Nothing But NET: a review of neuroendocrine tumors and carcinomas. *Neoplasia* (United States). 2017; 991–1002. [cited 2019 Dec 11]. Available from: <http://www.ncbi.nlm.nih.gov/pubmed/29091800>.
- Hofland J, Kaltsas G, de Herder WW. Advances in the diagnosis and management of well-differentiated neuroendocrine neoplasms. *Endocr Rev*. 2020;41:371–403.
- Gerlinger M, Rowan AJ, Horswell S, Larkin J, Endesfelder D, Gronroos E, et al. Intratumor heterogeneity and branched evolution revealed by multiregion sequencing. *N Engl J Med*. 2012;366:883–92 [cited 2019 Dec 11] Available from: <http://www.nejm.org/doi/abs/10.1056/NEJMoa1113205>.
- Ziv E, Durack JC, Solomon SB. The importance of biopsy in the era of molecular medicine. *Cancer J*. (United States). 2016. p. 418–22. [cited 2019 Dec 11] Available from: <http://www.ncbi.nlm.nih.gov/pubmed/27870685>.
- McQuery JA, Chang JT, Bowtell DDL, Cohen A, Bild AH. Mechanisms and clinical implications of tumor heterogeneity and convergence on recurrent phenotypes. *J. Mol. Med*. 2017; 1167–78. [cited 2019 Dec 11]. Available from: <http://www.ncbi.nlm.nih.gov/pubmed/28871446>.
- Grillo F, Albertelli M, Brisigotti MP, Borra T, Boschetti M, Fiocca R, et al. Grade increases in gastroenteropancreatic neuroendocrine tumor metastases compared to the primary tumor. *Neuroendocrinol*. 2016;103:452–9.
- Serkova NJ. Translational imaging endpoints to predict treatment response to novel targeted anticancer agents. *Drug Resist Updat*. 2011 [cited 2019 Dec 11];14:224–35. Available from: <http://www.ncbi.nlm.nih.gov/pubmed/21640633>.

8. James ML, Gambhir SS. A molecular imaging primer: modalities, imaging agents, and applications. *Physiol. Rev.* 2012 [cited 2019 Dec 11]. p. 897–965. Available from: <http://www.ncbi.nlm.nih.gov/pubmed/22535898>.
9. Jennings M, Marcu LG, Bezak E. PET-specific parameters and radiotracers in theoretical tumour modelling. *Comput Math Methods Med.* 2015 [cited 2019 Dec 11];2015:415923. Available from: <http://www.ncbi.nlm.nih.gov/pubmed/25788973>.
10. Tirosh A, Kebebew E. The utility of 68Ga-DOTATATE positron-emission tomography/computed tomography in the diagnosis, management, follow-up and prognosis of neuroendocrine tumors. *Futur Oncol.* 2018;14:111–22.
11. Giovannini E, Giovacchini G, Borsò E, Lazzeri P, Riondato M, Leoncini R, et al. [68 Ga]-Dota Peptide PET/CT in Neuroendocrine Tumors: Main Clinical Applications. *Curr Radiopharm.* 2018;12:11–22. [cited 2019 Dec 11] Available from: <http://www.eurekaselect.com/168288/article>.
12. Carideo L, Proserpi D, Panzuto F, Magi L, Pratesi MS, Rinzivillo M, et al. Role of Combined [68Ga]Ga-DOTA-SST analogues and [18F]FDG PET/CT in the management of GEP-NENs: a systematic review. *J Clin Med.* 2019 [cited 2019 Dec 11];8:1032. Available from: <https://www.mdpi.com/2077-0383/8/7/1032>.
13. Chan DLH, Pavlakis N, Schembri GP, Bernard EJ, Hsiao E, Hayes A, et al. Dual somatostatin receptor/FDG PET/CT imaging in metastatic neuroendocrine tumours: Proposal for a novel grading scheme with prognostic significance. *Theranostics.* 2017;7:1149–58.
14. Hatt M, Tixier F, Pierce L, Kinahan PE, Le Rest CC, Visvikis D. Characterization of PET/CT images using texture analysis: the past, the present... any future? *Eur. J. Nucl. Med. Mol.* 2017. 151–65.
15. Ha S, Choi H, Paeng JC, Cheon GJ. Radiomics in oncological PET/CT: a methodological overview. *Nucl. Med. Mol. Imaging* (2010). 2019 [cited 2019 Dec 11]. p. 14–29. Available from: <http://www.ncbi.nlm.nih.gov/pubmed/30828395>.
16. Lambin P, Rios-Velazquez E, Leijenaar R, Carvalho S, Van Stiphout RGPM, Granton P, et al. Radiomics: extracting more information from medical images using advanced feature analysis. *Eur J Cancer.* 2012;48:441–6.
17. Gillies RJ, Kinahan PE, Hricak H. Radiomics: images are more than pictures, they are data. *Radiol.* 2016;278:563–77.
18. Sanduleanu S, Woodruff HC, de Jong EEC, van Timmeren JE, Jochems A, Dubois L, et al. Tracking tumor biology with radiomics: a systematic review utilizing a radiomics quality score. *Radiother. Oncol.* 2018. p. 349–360.
19. Cook GJR, Azad G, Owczarczyk K, Siddique M, Goh V. Challenges and promises of PET radiomics. *Int J Radiat Oncol Biol Phys.* 2018;102:1083–9. [cited 2019 Dec 11] Available from: <http://www.ncbi.nlm.nih.gov/pubmed/29395627>.
20. Zwanenburg A. Radiomics in nuclear medicine: robustness, reproducibility, standardization, and how to avoid data analysis traps and replication crisis. *Eur J Nucl Med Mol Imaging.* 2019;46:2638–55. [cited 2019 Dec 11] Available from: <http://www.ncbi.nlm.nih.gov/pubmed/31240330>.
21. Castiglioni I, Gilardi MC. Radiomics: is it time to compose the puzzle? *Clin Transl Imaging.* 2018;6:411–3. [cited 2019 Dec 11] Available from: <http://www.ncbi.nlm.nih.gov/pubmed/30416989>.
22. Gatta R, Depeursinge A, Ratib O, Michielin O, Leimgruber A. Integrating radiomics into holomics for personalised oncology: from algorithms to bedside. *Eur. Radiol. Exp.* 2020.
23. Duron L, Balvay D, Perre S Vande, Bouchouicha A, Savatovsky J, Sadik JC, et al. Gray-level discretization impacts reproducible MRI radiomics texture features. *PLoS One.* 2019;14.
24. Mayerhoefer ME, Materka A, Langs G, Häggström I, Szczypiński P, Gibbs P, et al. Introduction to radiomics. *J. Nucl. Med. NLM (Medline)*; 2020. p. 488–95.
25. Traverso A, Wee L, Dekker A, Gillies R. Repeatability and reproducibility of radiomic features: a systematic review. *Int J Radiat Oncol Biol Phys.* 2018;102:1143–58.
26. Bailly C, Bodet-Milin C, Couespel S, Necib H, Kraeber-Bodéré F, Ansquer C, et al. Revisiting the robustness of PET-based textural features in the context of multi-centric trials. *PLoS One.* 2016;11:154–91.
27. Orhac F, Thézé B, Soussan M, Boisgard R, Buvat I. Multiscale texture analysis: from 18F-FDG PET images to histologic images. *J Nucl Med.* 2016;57:1823–8. [cited 2019 Dec 11] Available from: <http://www.ncbi.nlm.nih.gov/pubmed/27261515>.
28. Tixier F, Hatt M, Le Rest CC, Le Pogam A, Corcos L, Visvikis D. Reproducibility of tumor uptake heterogeneity characterization through textural feature analysis in 18F-FDG PET. *J Nucl Med. J Nucl Med.* 2012;53:693–700.
29. Leijenaar RTH, Carvalho S, Velazquez ER, Van Elmpst WJC, Parmar C, Hoekstra OS, et al. Stability of FDG-PET radiomics features: an integrated analysis of test-retest and inter-observer variability. *Acta Oncol (Madr).* 2013;52:1391–7.
30. van Velden FHP, Kramer GM, Frings V, Nissen IA, Mulder ER, de Langen AJ, et al. Repeatability of radiomic features in non-small-cell lung cancer [18F]FDG-PET/CT studies: impact of reconstruction and delineation. *Mol Imaging Biol.* 2016;18:788–95.
31. Weber WA, Gatsonis CA, David Mozley P, Hanna LG, Shields AF, Aberle DR, et al. Repeatability of 18F-FDG PET/CT in advanced non-small cell lung cancer: prospective assessment in 2 multicenter trials. *J Nucl Med.* 2015;56:1137–43.
32. Jodal L, Le Loirec C, Champion C. Positron range in PET imaging: an alternative approach for assessing and correcting the blurring. *Phys Med Biol.* 2012;57:3931–43. [cited 2020 Nov 22] Available from: <http://iopscience.iop.org/0031-9155/57/12/3931>.
33. Bailly C, Bodet-Milin C, Couespel S, Necib H, Kraeber-Bodéré F, Ansquer C, et al. Revisiting the robustness of PET-based textural features in the context of multi-centric trials. *PLoS One.* 2016;11:e0159984 [cited 2020 Feb 7] Available from: <http://www.ncbi.nlm.nih.gov/pubmed/27467882>.
34. Lindström E, Lindsjö L, Sundin A, Sörensen J, Lubberink M. Evaluation of block-sequential regularized expectation maximization reconstruction of 68Ga-DOTATOC, 18F-fluoride, and 11C-acetate whole-body examinations acquired on a digital time-of-flight PET/CT scanner. *EJNMMI Phys. Springer*; 2020 [cited 2020 Nov 18];7. Available from: <https://pubmed.ncbi.nlm.nih.gov/32542512/>.
35. Kroiss A, Putzer D, Decristoforo C, Uprimny C, Warwitz B, Nilica B, et al. 68Ga-DOTA-TOC uptake in neuroendocrine tumour and healthy tissue: Differentiation of physiological uptake and pathological processes in PET/CT. *Eur J Nucl Med Mol Imaging.* Eur J Nucl Med Mol Imaging; 2013 [cited 2020 Nov 22];40:514–23. Available from: <https://pubmed.ncbi.nlm.nih.gov/23291643/>.
36. Balon HR, Brown TLY, Goldsmith SJ, Silberstein EB, Krenning EP, Lang O, et al. The SNM practice guideline for somatostatin receptor scintigraphy 2.0. *J Nucl Med Technol.* 2011;39:317–24.
37. Oberg K, Modlin IM, De Herder W, Pavel M, Klimstra D, Frilling A, et al. Consensus on biomarkers for neuroendocrine tumour disease. *Lancet Oncol.* 2015; e435–46.

38. Bozkurt MF, Virgolini I, Balogova S, Beheshti M, Rubello D, Decristoforo C, et al. Guideline for PET/CT imaging of neuroendocrine neoplasms with <sup>68</sup>Ga-DOTA-conjugated somatostatin receptor targeting peptides and <sup>18</sup>F-DOPA. *Eur J Nucl Med Mol Imaging*. 2017;44:1588–601.
39. Nioche C, Orlhac F, Boughdad S, Reuze S, Goya-Outi J, Robert C, et al. Lifex: a freeware for radiomic feature calculation in multimodality imaging to accelerate advances in the characterization of tumor heterogeneity. *Cancer Res*. 2018;78:4786–9.
40. Chan TF, Vese LA. Active contours without edges. *IEEE Trans Image Process*. 2001;10:266–77.
41. Torihara A, Baratto L, Nobashi T, Park S, Hatami N, Davidzon G, et al. Prognostic value of somatostatin receptor expressing tumor volume calculated from <sup>68</sup>Ga-DOTATATE PET/CT in patients with well-differentiated neuroendocrine tumors. *Eur J Nucl Med Mol Imaging*. 2019;46:2244–51.
42. Foster B, Bagci U, Mansoor A, Xu Z, Mollura DJ. A review on segmentation of positron emission tomography images. *Comput. Biol. Med*; 2014. p. 76–96.
43. Boellaard R, Delgado-Bolton R, Oyen WJG, Giammarile F, Tatsch K, Eschner W, et al. FDG PET/CT: EANM procedure guidelines for tumour imaging: version 2.0. *Eur. J. Nucl. Med. Mol. Imaging*. 2015. p. 328–54.
44. Zwanenburg A, Leger S, Vallières M, Löck S. Image biomarker standardisation initiative. 2016 [cited 2020 Jan 10]; Available from: <http://arxiv.org/abs/1612.07003>.
45. Leijenaar RTH, Nalbantov G, Carvalho S, Van Elmpot WJC, Troost EGC, Boellaard R, et al. The effect of SUV discretization in quantitative FDG-PET Radiomics: the need for standardized methodology in tumor texture analysis. *Sci Rep*. 2015;5:1–10.
46. Orlhac F, Soussan M, Chouahnia K, Martinod E, Buvat I. <sup>18</sup>F-FDG PET-derived textural indices reflect tissue-specific uptake pattern in non-small cell lung cancer. *PLoS One. Public Library of Science*; 2015 [cited 2020 Feb 18];10:e0145063. Available from: <http://www.ncbi.nlm.nih.gov/pubmed/26669541>.
47. Orlhac F, Nioche C, Soussan M, Buvat I. Understanding changes in tumor texture indices in PET: a comparison between visual assessment and index values in simulated and patient data. *J Nucl Med*; 2017;58:387–92. [cited 2020 Feb 18] Available from: <http://www.ncbi.nlm.nih.gov/pubmed/27754906>.
48. Warfield SK, Zou KH, Wells WM. Simultaneous truth and performance level estimation (STAPLE): an algorithm for the validation of image segmentation. *IEEE Trans Med Imaging*. 2004;23:903–21.
49. Koo TK, Li MY. A guideline of selecting and reporting intraclass correlation coefficients for reliability research. *J Chiropr Med. Elsevier USA*. 2016;15:155–63.
50. Pfaehler E, van Sluis J, Merema BBJ, van Ooijen P, Berendsen RCM, van Velden FHP, et al. Experimental multicenter and multivendor evaluation of the performance of PET radiomic features using 3-dimensionally printed phantom inserts. *J Nucl Med. NLM (Medline)*; 2020;61:469–76.
51. Rfsc. R: A language and environment for statistical computing. 2008 [cited 2020 Feb 28]. Available from: <https://www.gbif.org/tool/81287/r-a-language-and-environment-for-statistical-computing>.
52. Altazi BA, Zhang GG, Fernandez DC, Montejo ME, Hunt D, Werner J, et al. Reproducibility of <sup>18</sup>F-FDG PET radiomic features for different cervical tumor segmentation methods, gray-level discretization, and reconstruction algorithms. *J Appl Clin Med Phys*. 2017;18:32–48.
53. Bashir U, Azad G, Siddique MM, Dhillon S, Patel N, Bassett P, et al. The effects of segmentation algorithms on the measurement of <sup>18</sup>F-FDG PET texture parameters in non-small cell lung cancer. *EJNMMI Res*. 2017;7.
54. Biehl KJ, Kong FM, Dehdashti F, Jin JY, Mutic S, El Naqa I, et al. <sup>18</sup>F-FDG PET definition of gross tumor volume for radiotherapy of non-small cell lung cancer: is a single standardized uptake value threshold approach appropriate? *Society of Nuclear Medicine*. 2006;47:1808–12.
55. Werner RA, Lapa C, Ilhan H, Higuchi T, Buck AK, Lehner S, et al. Survival prediction in patients undergoing radionuclide therapy based on intratumoral somatostatin-receptor heterogeneity. *Oncotarget*. 2017;8:7039–49 [cited 2020 Feb 7] Available from: <http://www.ncbi.nlm.nih.gov/pubmed/27705948>.
56. Werner RA, Ilhan H, Lehner S, Papp L, Zsótér N, Schatka I, et al. Pre-therapy Somatostatin receptor-based heterogeneity predicts overall survival in pancreatic neuroendocrine tumor patients undergoing peptide receptor radionuclide therapy. *Mol Imaging Biol*. 2019;21:582–90.
57. Weber M, Kessler L, Schaarschmidt B, Fendler WP, Lahner H, Antoch G, et al. Textural analysis of hybrid DOTATOC-PET/MRI and its association with histological grading in patients with liver metastases from neuroendocrine tumors. *Nucl Med Commun*. 2020;41:363–9 [cited 2020 Oct 6] Available from: <https://pubmed.ncbi.nlm.nih.gov/31977752/>.
58. Weber M, Kessler L, Schaarschmidt B, Fendler WP, Lahner H, Antoch G, et al. Treatment-related changes in neuroendocrine tumors as assessed by textural features derived from <sup>68</sup>Ga-DOTATOC PET/MRI with simultaneous acquisition of apparent diffusion coefficient. *BMC Cancer*; 2020 [cited 2020 Oct 6];20. Available from: <https://pubmed.ncbi.nlm.nih.gov/32299391/>.
59. Werner-Wasik M, Nelson AD, Choi W, Arai Y, Faulhaber PF, Kang P, et al. What is the best way to contour lung tumors on PET scans? Multiobserver validation of a gradient-based method using a NSCLC digital PET phantom. *Int J Radiat Oncol Biol Phys*. 2012;82:1164–71.
60. Halt M, Le Rest CC, Turzo A, Roux C, Visvikis D. A fuzzy locally adaptive Bayesian segmentation approach for volume determination in PET. *IEEE Trans Med Imaging*. 2009;28:881–93.
61. Parmar C, Leijenaar RTH, Grossmann P, Velazquez ER, Bussink J, Rietveld D, et al. Radiomic feature clusters and prognostic signatures specific for lung and head & neck cancer. *Sci Rep*. 2015;5.
62. Messerli M, Kotasidis F, Burger IA, Ferraro DA, Muehlethaler UJ, Weyeremann C, et al. Impact of different image reconstructions on PET quantification in non-small cell lung cancer: a comparison of adenocarcinoma and squamous cell carcinoma. *Br J Radiol*. 2019;92.
63. Lu L, Lv W, Jiang J, Ma J, Feng Q, Rahmim A, et al. Robustness of radiomic features in [<sup>11</sup>C]choline and [<sup>18</sup>F]FDG PET/CT imaging of nasopharyngeal carcinoma: impact of segmentation and discretization. *Mol Imaging Biol*. 2016;18:935–45.
64. Binderup T, Knigge U, Loft A, Federspiel B, Kjaer A. <sup>18</sup>F-fluorodeoxyglucose positron emission tomography predicts survival of patients with neuroendocrine tumors. *Clin Cancer Res. Clin Cancer Res*. 2010;16:978–85.
65. Oberg K, Krenning E, Sundin A, Bodei L, Kidd M, Tesselar M, et al. A delphic consensus assessment: imaging and biomarkers in gastroenteropancreatic neuroendocrine tumor disease management. *Endocr Connect*. 2016;5:174–87. [cited 2020 Feb 7] Available from: <http://www.ncbi.nlm.nih.gov/pubmed/27582247>.

66. Radiomics: the bridge between medical imaging and personalized medicine. - PubMed - NCBI. [cited 2020 Feb 7]. Available from: <https://www.ncbi.nlm.nih.gov/pubmed/?term=Lambin++Radiomics%3A+the+bridge+between+medical+imaging+and+personalized+medicine>.
67. Geets X, Lee JA, Bol A, Lonneux M, Grégoire V. A gradient-based method for segmenting FDG-PET images: Methodology and validation. *Eur J Nucl Med Mol Imaging*. 2007;34:1427–38. [cited 2020 Jan 9] Available from: <http://www.ncbi.nlm.nih.gov/pubmed/17431616>.

### **Publisher's Note**

Springer Nature remains neutral with regard to jurisdictional claims in published maps and institutional affiliations.

**Submit your manuscript to a SpringerOpen<sup>®</sup> journal and benefit from:**

- ▶ Convenient online submission
- ▶ Rigorous peer review
- ▶ Open access: articles freely available online
- ▶ High visibility within the field
- ▶ Retaining the copyright to your article

---

Submit your next manuscript at ▶ [springeropen.com](https://www.springeropen.com)

---